



Universiteit  
Leiden  
The Netherlands

## A direct calibration of the IRX- $\beta$ relation in Lyman-break Galaxies at $z = 3-5$

Koprowski, M.P.; Coppin, K.E.K.; Geach, J.E.; McLure, R.J.; Almaini, O.; Blain, A.W.; ... ; Werf, P.P. van der

### Citation

Koprowski, M. P., Coppin, K. E. K., Geach, J. E., McLure, R. J., Almaini, O., Blain, A. W., ... Werf, P. P. van der. (2018). A direct calibration of the IRX- $\beta$  relation in Lyman-break Galaxies at  $z = 3-5$ . *Monthly Notices Of The Royal Astronomical Society*, 479(4), 4355-4366. doi:10.1093/mnras/sty1527

Version: Not Applicable (or Unknown)

License: [Leiden University Non-exclusive license](#)

Downloaded from: <https://hdl.handle.net/1887/71090>

**Note:** To cite this publication please use the final published version (if applicable).

# A direct calibration of the IRX- $\beta$ relation in Lyman-break Galaxies at $z=3-5$

M. P. Koprowski<sup>1\*</sup>, K. E. K. Coppin<sup>1</sup>, J. E. Geach<sup>1</sup>, R. J. McLure<sup>2</sup>, O. Almaini<sup>3</sup>,  
 A. W. Blain<sup>4</sup>, M. Bremer<sup>5</sup>, N. Bourne<sup>2</sup>, S. C. Chapman<sup>6</sup>, C. J. Conselice<sup>7</sup>, J. S. Dunlop<sup>2</sup>,  
 D. Farrah<sup>8</sup>, W. Hartley<sup>9</sup>, A. Karim<sup>10</sup>, K. K. Knudsen<sup>11</sup>, M. J. Michałowski<sup>12</sup>,  
 D. Scott<sup>13</sup>, C. Simpson<sup>14</sup>, D. J. B. Smith<sup>1</sup>, P. P. van der Werf<sup>15</sup>,

<sup>1</sup>Centre for Astrophysics Research, School of Physics, Astronomy and Mathematics, University of Hertfordshire, College Lane, Hatfield AL10 9AB,

<sup>2</sup>Institute for Astronomy, University of Edinburgh, Royal Observatory, Edinburgh EH9 3HJ, UK

<sup>3</sup>School of Physics and Astronomy, University of Nottingham, University Park, Nottingham NG7 2RD, UK

<sup>4</sup>Physics & Astronomy, University of Leicester, 1 University Road, Leicester LE1 7RH, UK

<sup>5</sup>Astrophysics Group, School of Physics, University of Bristol, Tyndall Avenue, Bristol BS8 1TL, UK

<sup>6</sup>Department of Physics and Atmospheric Science, Dalhousie University, Halifax, NS B3H 4R2, Canada

<sup>7</sup>University of Nottingham, School of Physics & Astronomy, Nottingham, NG7 2RD, UK

<sup>8</sup>Department of Physics, Virginia Tech, Blacksburg, VA 24061, USA

<sup>9</sup>Department of Physics and Astronomy, University College London, London, WC1E 6BT, UK

<sup>10</sup>Argelander-Institut für Astronomie, Universität Bonn, Auf dem Hügel 71, D-53121 Bonn, Germany

<sup>11</sup>Department of Space, Earth and Environment, Chalmers University of Technology, Onsala Space Observatory, SE-43992 Onsala, Sweden

<sup>12</sup>Astronomical Observatory Institute, Faculty of Physics, Adam Mickiewicz University, ul. Stoleczna 36, 60-286 Poznań, Poland

<sup>13</sup>Department of Physics and Astronomy, 6224 Agricultural Road, University of British Columbia, Vancouver V6T 1Z1, Canada

<sup>14</sup>Gemini Observatory, Northern Operations Center, 670 N. A'ohuku Place, Hilo, HI 96720, USA

<sup>15</sup>Leiden Observatory, Leiden University, P.O. Box 9513, NL-2300 RA Leiden, The Netherlands

Accepted XXX. Received YYY; in original form ZZZ

## ABSTRACT

We use a sample of 4178 Lyman break galaxies (LBGs) at  $z \simeq 3, 4$  and  $5$  in the UKIRT Infrared Deep Sky Survey (UKIDSS) Ultra Deep Survey (UDS) field to investigate the relationship between the observed slope of the stellar continuum emission in the ultraviolet,  $\beta$ , and the thermal dust emission, as quantified via the so-called ‘infrared excess’ ( $\text{IRX} \equiv L_{\text{IR}}/L_{\text{UV}}$ ). Through a stacking analysis we directly measure the  $850\mu\text{m}$  flux density of LBGs in our deep (0.9 mJy) James Clerk Maxwell Telescope (JCMT) SCUBA-2  $850\mu\text{m}$  map, as well as deep public *Herschel*/SPIRE 250-, 350- and  $500\mu\text{m}$  imaging. We establish functional forms for the IRX- $\beta$  relation to  $z \sim 5$ , confirming that there is no significant redshift evolution of the relation and that the resulting average IRX- $\beta$  curve is consistent with a Calzetti-like attenuation law. We compare our results with recent work in the literature, finding that discrepancies in the slope of the IRX- $\beta$  relation are driven by biases in the methodology used to determine the ultraviolet slopes. Consistent results are found when IRX- $\beta$  is evaluated by stacking in bins of stellar mass, and we argue that the near-linear IRX- $M_{\star}$  relationship is a better proxy for correcting observed UV luminosities to total star formation rates, provided an accurate handle on  $M_{\star}$  can be had, and also gives clues as to the physical driver of the role of dust-obscured star formation in high-redshift galaxies.

**Key words:** dust, extinction – galaxies: evolution, high-redshift, star formation, ISM – cosmology: observations

## 1 INTRODUCTION

Understanding the evolution of the star formation rate density (SFRD) with cosmic time has long been the cornerstone of extragalactic astrophysics (e.g. [Madau & Dickinson](#)

\* E-mail: m.koprowski@herts.ac.uk

2014). At  $z > 2$  most studies of the evolution of the SFRD are based on samples of Lyman-break galaxies (LBGs), due in part because of the efficiency of their selection technique in deep broad band imaging surveys.

As a result, LBGs have been extensively studied and well-characterised over the past two decades. They have stellar masses  $\sim 10^9\text{--}10^{11} M_\odot$  and star formation rates (SFRs)  $\sim 10\text{--}100 M_\odot \text{y}^{-1}$ , (e.g. Madau et al. 1996; Steidel et al. 1996; Sawicki & Yee 1998; Shapley et al. 2001; Giavalisco 2002; Blaizot et al. 2004; Shapley et al. 2005; Reddy et al. 2006; Rigopoulou et al. 2006; Verma et al. 2007; Magdis et al. 2008; Stark et al. 2009; Chapman & Casey 2009; Lo Faro et al. 2009; Magdis et al. 2010; Rigopoulou et al. 2010; Pentericci et al. 2010; Oteo et al. 2013; Bian et al. 2013). LBGs are therefore believed to be responsible for forming a substantial fraction of massive local galaxies ( $L > L^*$ ; e.g. Somerville et al. 2001; Baugh et al. 2005), while those with the highest SFRs ( $> 100 M_\odot \text{y}^{-1}$ ) could be the progenitors of present-day ellipticals (e.g. Verma et al. 2007; Stark et al. 2009; Reddy & Steidel 2009).

Naturally, given their selection, the most common tracer of LBGs' SFRs has traditionally been through their rest-frame UV stellar continuum emission (e.g. Kennicutt & Evans 2012). However, it is now well known that about half of the starlight in the Universe is absorbed by interstellar dust and re-emitted in the rest-frame far-infrared (e.g. Dole et al. 2006). It is therefore necessary to complement UV-derived SFRs with far-infrared and sub-millimetre observations to obtain a full census of star formation, with the latter providing the most efficient probe of thermal dust emission out to high redshift owing to the negative k-correction. Unfortunately, typical LBGs are faint in the sub-millimetre, far below the confusion limit of most single-dish sub-millimetre facilities and challenging even for sensitive interferometric facilities such as the Atacama Large Millimeter/sub-millimeter Array (ALMA) (Chapman et al. 2000; Capak et al. 2015; Bouwens et al. 2016; Koprowski et al. 2016; Dunlop et al. 2017; McLure et al. 2017). As a result, representative samples of sub-millimeter-detected LBGs are not available.

Without direct detection of the obscured star formation in individual LBGs, empirical recipes are used to correct UV-derived SFRs to total SFRs. The most common approach is to use the relationship between the rest-frame UV slope,  $\beta$ , where  $f_\lambda \propto \lambda^\beta$ , and the infrared excess,  $\text{IRX} \equiv L_{\text{IR}}/L_{\text{UV}}$  (Meurer et al. 1999). Overzier et al. (2011) found that local analogues of LBGs are consistent with the Meurer et al. (1999) relation, while at ( $z \gtrsim 3$ ) Coppin et al. (2015) and Álvarez-Márquez et al. (2016) found LBGs to be lying above and below the local relation respectively. Recently, McLure et al. (2017) showed that the IRX- $\beta$  relation for  $z \sim 3$  galaxies is consistent with a Calzetti-like attenuation law (Calzetti et al. 2000), while Reddy et al. (2017) suggest that a flatter, Small Magellanic Cloud (SMC)-like curve should be applied. In addition, a number of individual direct detections for LBGs and infrared-selected galaxies, have been found to exhibit a large scatter in the IRX- $\beta$  plane (Casey et al. 2014; Capak et al. 2015; Scoville et al. 2016; Koprowski et al. 2016; Fudamoto et al. 2017). It remains unclear whether these inconsistencies are due to intrinsic scatter in the IRX- $\beta$  relation or biases in the selection and measurement technique. In either case, it is important to

re-evaluate the IRX- $\beta$  relation for high- $z$  LBGs if we wish to use it for the accurate correction of UV-derived SFRs where direct infrared detection is not available.

In this paper we make use of a large sample of LBGs at redshifts  $3 < z < 5$  in the UKIDSS/UDS field, stellar mass complete down to a limit of  $\log(M_*/M_\odot) \gtrsim 10.0$ , to establish the IRX- $\beta$  relation. We are able to determine the IR luminosities for these galaxies through stacking of a deep JCMT SCUBA-2 850  $\mu\text{m}$  map from the SCUBA-2 Cosmology Legacy Survey (Geach et al. 2017), and 350–500  $\mu\text{m}$  SPIRE mapping from the *Herschel Space Observatory*. This paper expands on the work of Coppin et al. (2015), with an improved SCUBA-2 map of UDS, now approaching the SCUBA-2 confusion limit (with a  $1\sigma$  depth of  $0.9 \text{ mJy beam}^{-1}$ ). Section 2 summarises the data used and explains our LBG selection criteria. In Section 3 we explain how the spectral energy distribution (SED) fitting is performed and derive the basic physical properties of galaxies in the sample. In Section 4 we measure the IRX- $\beta$  relation for LBGs at  $z = 3, 4$  and  $5$  and explain its physical origin, comparing our findings with other results from the literature. We present our conclusions in Section 5.

Throughout, magnitudes are quoted in the AB system (Oke & Gunn 1983) and we use the Chabrier (2003) stellar initial mass function (IMF). We assume a cosmology with  $\Omega_m = 0.3$ ,  $\Omega_\Lambda = 0.7$  and  $H_0 = 70 \text{ km s}^{-1} \text{ Mpc}^{-1}$ . We note that assuming the best-fit Planck Collaboration et al. (2016) cosmology yields  $\simeq 2\text{--}2.5\%$  higher luminosity distances and hence  $\simeq 4\text{--}5\%$  higher stellar masses and luminosities.

## 2 DATA

### 2.1 Optical & near-IR imaging

Our sample is drawn from the deep  $K$ -band image of the UKIRT Infrared Deep Sky Survey (UKIDSS; Lawrence et al. 2007), UDS<sup>1</sup> data release 8 (DR8), together with the available multi-wavelength photometry. The UDS is the deepest of the five UKIDSS sub-surveys (Almaini et al., in prep.), covering  $0.77 \text{ deg}^2$  in the  $J, H$  and  $K$  bands. The DR8 release achieves  $5\sigma$  point source depths of 24.9, 24.2 and 24.6 mag, respectively. The parent catalogue was extracted from the  $K$ -band image using SExtractor (Bertin & Arnouts 1996). Two catalogues were constructed and merged: the first was designed to extract point sources, while the second was optimized to detect resolved galaxies (see Hartley et al. 2013 for details). The UKIDSS UDS has also been imaged by the Canada-France-Hawaii Telescope (CFHT) Megacam  $U$ -band (26.75 mag), Subaru Suprime-cam ( $B = 27.6$ ,  $V = 27.2$ ,  $R = 27.0$ ,  $i' = 27.0$ , and  $z' = 26.0$ ; Furusawa et al. 2008) and the *Spitzer* Infrared Array Camera (IRAC; Fazio et al. 2004,  $[3.6\mu\text{m}] = 24.2$  and  $[4.5\mu\text{m}] = 24.0$ ), as a part of the UDS *Spitzer* Legacy Program (SpUDS; PI: Dunlop). To remove obvious active galactic nuclei (AGN), X-ray (Ueda et al. 2008) and radio (Simpson et al. 2006) data were used. The total coincident area of these data sets is  $0.62 \text{ deg}^2$ . All images were astrometrically aligned and multi-band photometry extracted in 3-arcsec diameter apertures at the positions

<sup>1</sup> <http://www.nottingham.ac.uk/astronomy/UDS/>

of  $K$ -band detections (see [Simpson et al. 2012](#) for details), including point spread function corrections where appropriate ([Hartley et al. 2013](#)).

### 2.1.1 LBG selection

The LBG selection technique relies on the fact that photons with energies higher than the rest-frame 1216 are almost entirely absorbed by the neutral gas around the star-forming regions in the galaxy. This results in the characteristic break which can be easily identified with broadband colours. This technique is primarily used to identify galaxies at  $z \approx 3$  using  $UGR$ , or  $BVR$ , filters ([Steidel et al. 1996](#)), but can be easily extended to higher redshifts by simply shifting the colour space to longer wavelengths, as described by [Ouchi et al. \(2004\)](#). In this work we use the following selections for LBGs at  $z \approx 3$  (Equation 1),  $z \approx 4$  (Equation 2) and  $z \approx 5$  (Equations 3 and 4):

$$\begin{aligned} R < 27, & & (U - V) > 1.2, \\ -1.0 < (V - R) < 0.6, & & (U - V) > 3.8(V - R) + 1.2; \end{aligned} \quad (1)$$

$$\begin{aligned} i' < 27, & & (B - R) > 1.2, \\ (R - i') < 0.7, & & (B - R) > 1.6(R - i') + 1.9; \end{aligned} \quad (2)$$

$$\begin{aligned} z' < 26, & & (V - i') > 1.2, \\ (i' - z') < 0.7, & & (V - i') > 1.8(i' - z') + 2.3; \end{aligned} \quad (3)$$

$$\begin{aligned} z' < 26, & & (R - i') > 1.2, \\ (i' - z') < 0.7, & & (R - i') > (i' - z') + 1.0, \end{aligned} \quad (4)$$

where  $z \approx 5$  LBGs are identified using either Equation 3 or 4 in order to maximise our yield (see [Ouchi et al. 2004](#)). Note that, since the parent optical catalogue is selected at  $K$ -band ( $K < 24.6$ ), our resulting LBG sample is mass complete to a limit of  $\log(M_*/M_\odot) \gtrsim 10.0$ .

Photometric redshifts are determined for each source in our parent catalogue using 11 photometry bands ( $UBVRi'z'JHK[3.6][4.5]$ ), as described in [Hartley et al. \(2013\)](#) and [Mortlock et al. \(2013\)](#), using the EAZY template-fitting code. Six SED templates were used ([Brammer et al. 2008](#)), with the bluest template having a SMC-like extinction added. The accuracy of the photometric redshifts is assessed by comparing with the available spectroscopic data, as described in [Hartley et al. \(2013\)](#), with the average  $|z_{\text{phot}} - z_{\text{spec}}|/(1 + z_{\text{spec}}) = 0.031$ .

To help eliminate low redshift interlopers in the LBG selections, we initially enforce the minimum best-fit (i.e. peak of the redshift probability density distribution) redshift to be  $z = 2$ . In the left panel of Figure 1 the normalised sum of the redshift probability distributions are shown for each redshift selection, indicating peaks at 3.35, 3.87 and 4.79. Thus, the selection criteria used here selects galaxies at redshifts consistent with the target values. However, all three distributions show a minor peak at  $z \approx 2.5$ , indicating contamination still present in the selection. To remedy this situation, we further enforce the maximum likelihood redshifts ( $z_{\text{best}}$ ) to be  $z > 2.5$ ,  $z > 3$  and  $z > 4$  for the  $z \approx 3$ ,  $z \approx 4$  and  $z \approx 5$  samples, respectively. This results in much ‘cleaner’ redshift probability distributions containing 3419, 699 and 60 sources

at mean redshifts of 3.35, 3.87 and 4.79, respectively. For the reasons explained in the next Section, we exclude 36 LBGs that are directly detected in the rest-frame FIR in high-resolution ALMA follow-up of all S2CLS-detected 850  $\mu\text{m}$  sources in the UDS field (PI: Smail). A detailed study of these ALMA-detected LBGs will be presented in [Koprowski et al. \(in preparation\)](#).

## 2.2 IR & sub-mm imaging

### 2.2.1 Spitzer MIPS & Herschel SPIRE data

We utilise mid-IR imaging from the Multiband Imaging Photometer for *Spitzer* instrument (MIPS; [Rieke et al. 2004](#)) at 24  $\mu\text{m}$  from the *Spitzer* Public Legacy Survey of the UKIDSS Ultra Deep Survey (SpUDS; PI: J. Dunlop), as described in [Caputi et al. \(2011\)](#), and sub-millimetre imaging from *Herschel* ([Pilbratt et al. 2010](#)), as provided by the public release of the HerMES ([Oliver et al. 2012](#)) survey undertaken with the SPIRE ([Griffin et al. 2010](#)) instrument, at 250, 350 and 500  $\mu\text{m}$ . The Level 2 data products from the *Herschel* European Space Agency (ESA) archive were retrieved, aligned and co-added to produce maps. The SPIRE maps are confused, and so we apply a de-blending procedure following [Swinbank et al. \(2014\)](#) using sources in the 24  $\mu\text{m}$  catalogue as priors for the positions of sources contributing to the SPIRE map. In brief, the optimal sky model is found assuming 24  $\mu\text{m}$  sources contribute to SPIRE sources detected at  $>2\sigma$  at 250  $\mu\text{m}$  and 350  $\mu\text{m}$  by minimising the residual flux density between a (PSF-convolved) sky model and the data. The best fitting 24  $\mu\text{m}$  sources are then subtracted from the SPIRE maps, excluding those actually associated with LBGs in our samples. This minimises the contribution to the stacked flux at the position of LBGs from confused SPIRE sources.

In addition, we have also decided to remove all the SPIRE-detected sources. This is motivated by the fact that the most IR-bright galaxies will lie significantly above the IRX- $\beta$  relation and hence a simple dust-screen model used in the derivation of the functional form of the relation ([Meurer et al. 1999](#)) cannot be applied to them. [Casey et al. \(2014\)](#) found that virtually all the galaxies with the IR luminosity  $\log(L_{\text{IR}}/L_\odot) \gtrsim 11.5$  have their IRX values significantly elevated above the local IRX- $\beta$  relation. With our average SEDs found in Section 3.1, we find that all the LBGs detected at SPIRE bands will satisfy the above criterion and hence the removal of all the SPIRE-detected sources is well motivated.

We have therefore excluded all the SPIRE galaxies from the maps, but we note that leaving the sources associated with our LBGs in increases the resulting values of IRX only by  $\sim 20\%$ . The resulting stacked SPIRE flux densities with errors are given in Table 1.

### 2.2.2 JCMT SCUBA-2 data

We use the final, near-confusion-limited 850  $\mu\text{m}$  map of the UDS from the SCUBA-2 Cosmology Legacy Survey (S2CLS). Full details of the observations and data reduction are given in [Geach et al. \(2017\)](#), but the map spans 1 degree centred on the UDS and reaches a uniform depth of 0.9 mJy beam $^{-1}$ . Note that this final map is a factor of 2

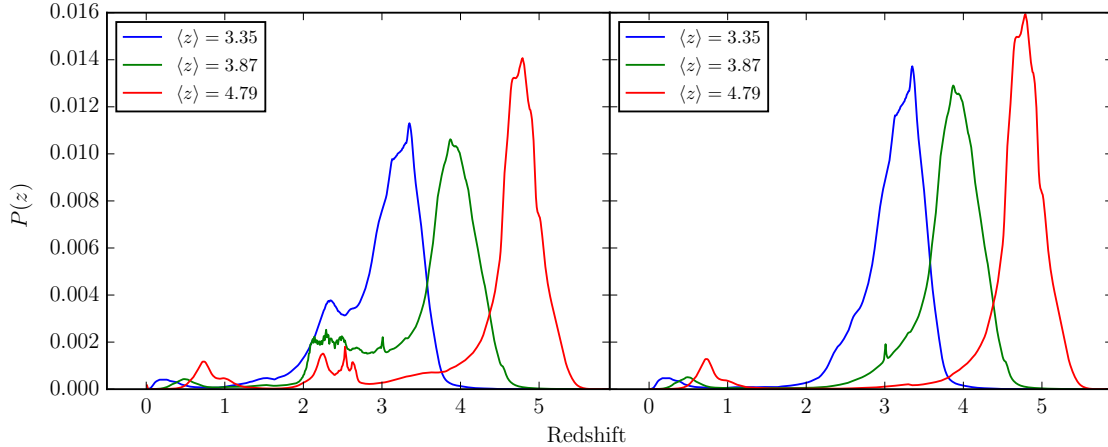


**Figure 1.** Redshift probability distributions with the corresponding most-probable redshifts shown in the legend. **Left:** Redshift probability distributions for the LBG selection criteria from Equations 1-4, with the additional constraint of  $z > 2$  in place. It can be seen that the resulting most-probable redshifts are close to the target values of 3, 4 and 5. However, the distributions show a low-redshift peak at  $z \approx 2.5$ , this being the result of a number of contaminating galaxies being included using our selection criteria. **Right:** Since the  $z \approx 2.5$  sources from the left panel will contaminate the inferred values of the stellar masses, as well as UV slopes, we decided to introduce an additional selection criteria, where we force the redshifts to be  $> 2.5$ ,  $> 3$  and  $> 4$  for the  $z \sim 3$ ,  $z \sim 4$  and  $z \sim 5$  samples, respectively. This panel shows the resulting redshift probability distributions. Note that the low-redshift peaks at  $z \sim 0.5$  do not result from a number of sources being found at low redshifts, but rather from a small number of individual probability distributions being double-peaked (with the low- $z$  solution having lower probability).

**Table 1.** Stacked IR-submm photometry for LBGs. The columns show the most-probable redshift in each bin, the number of selected LBGs and the stacked photometry in the *Herschel* SPIRE and JCMT SCUBA-2  $850\ \mu\text{m}$  bands, with  $1\sigma$  errors and detection significance in brackets.

$\langle z_{\text{phot}} \rangle$	$N$	$S_{250}$ / mJy	$S_{350}$ / mJy	$S_{500}$ / mJy	$S_{850}^a$ / mJy	$S_{850}^b$ / mJy
3.35	3419	$0.534 \pm 0.076$ (7.0 $\sigma$ )	$0.668 \pm 0.077$ (8.7 $\sigma$ )	$0.360 \pm 0.085$ (5.5 $\sigma$ )	$0.181 \pm 0.015$ (12.1 $\sigma$ )	$0.128 \pm 0.015$ (8.5 $\sigma$ )
3.87	699	$0.533 \pm 0.162$ (3.3 $\sigma$ )	$0.957 \pm 0.171$ (5.6 $\sigma$ )	$0.966 \pm 0.185$ (5.5 $\sigma$ )	$0.369 \pm 0.033$ (11.2 $\sigma$ )	$0.261 \pm 0.033$ (7.9 $\sigma$ )
4.79	60	$0.294 \pm 0.556$ (0.5 $\sigma$ )	$0.485 \pm 0.573$ (0.8 $\sigma$ )	$0.517 \pm 0.618$ (0.9 $\sigma$ )	$0.417 \pm 0.110$ (3.8 $\sigma$ )	$0.335 \pm 0.110$ (3.0 $\sigma$ )

<sup>a</sup> Mean weighted stack with the ALMA-detected LBGs present.

<sup>b</sup> Mean weighted stack with the ALMA-detected LBGs removed from the  $850\ \mu\text{m}$  map. We use this column for SED fitting.

deeper than the map used in Coppin et al. (2015). We subtracted all SCUBA-2 sources with the signal-to-noise ratio (SNR) of  $> 3.5$  from the  $850\text{-}\mu\text{m}$  maps following the same reasoning as the de-blending procedure used in the SPIRE maps.

We evaluate the stacked flux density of LBGs in SCUBA-2 and SPIRE maps following an inverse variance weighting:

$$\langle S_{\nu} \rangle = \frac{\sum_i^N S_{\nu,i} / \sigma_i^2}{\sum_i^N 1 / \sigma_i^2}, \quad (5)$$

where  $S_{\nu,i}$  is the flux density of the  $i$ th LBG and  $\sigma_i$  is the  $1\sigma$  instrumental noise at the same position. We assume that confusion noise is constant over the field. The error on the mean is then found from

$$\sigma^2(\langle S_{\nu} \rangle) = \frac{1}{\sum_i^N 1 / \sigma_i^2}. \quad (6)$$

We show thumbnail images in Figure 2 presenting the

inverse-variance weighted  $850\ \mu\text{m}$  stacks at the positions of LBGs in the three redshift bins, and list the average flux densities in Table 1. We find  $8.5\sigma$ ,  $7.9\sigma$  and  $3.0\sigma$  detections in the  $z \approx 3$ ,  $z \approx 4$  and  $z \approx 5$  redshift bins, respectively. Table 1 also gives the stacked SPIRE flux densities where we measure significant stacked detections in all but the  $z \approx 5$  bin.

Figure 3 shows the average radial profile of the  $z \approx 3$  stack compared to the SCUBA-2 beam (which differs slightly from a pure Gaussian). The stacked profile is indistinguishable from the shape of the beam and therefore any clustering of sources associated with the LBGs that also contribute to the  $850\ \mu\text{m}$  flux density (Chary & Pope 2010; Kurczynski & Gawiser 2010; Serjeant et al. 2010) are on scales unresolved by SCUBA-2; i.e. below approximately  $15''$  or 120 kpc. We ignore this potential contribution in the following analysis and consider the average submillimetre emission as coming from the LBG itself.

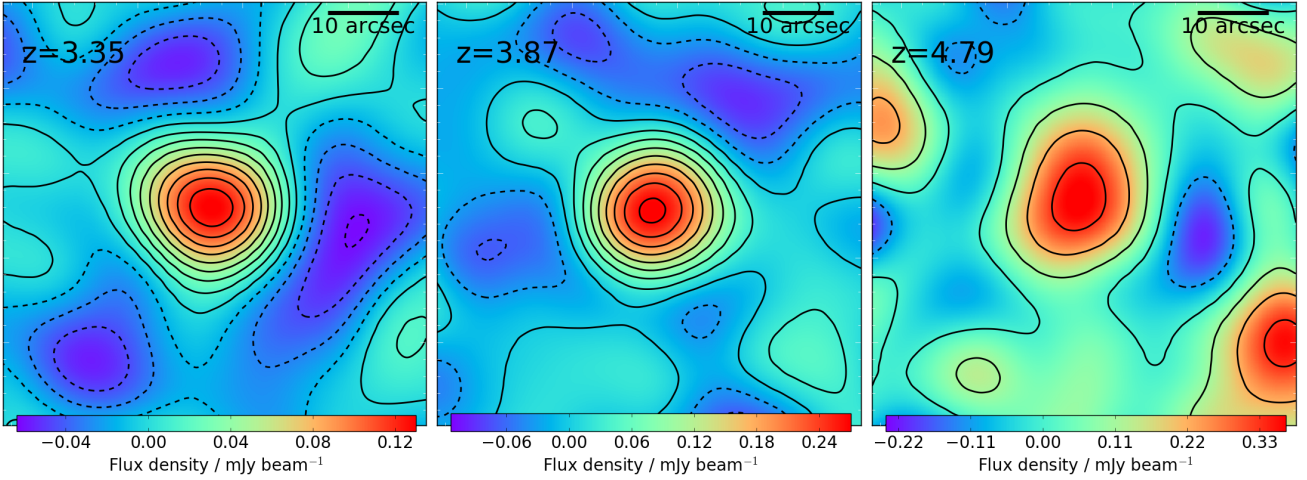


**Figure 2.** 60 arcsec  $\times$  60 arcsec stamps of the stacked 850  $\mu$ m flux densities in the SCUBA-2 maps for each redshift bin, centred on the LBG positions. The solid contours represent significance levels of  $0\sigma$ ,  $1\sigma$ ,  $2\sigma$ ,  $\dots$ , while the dashed lines show negative deviations. We find significant detections in each redshift bin, with amplitudes  $8.5\sigma$ ,  $7.9\sigma$  and  $3.0\sigma$  at  $z = 3.36$ ,  $z = 3.87$  and  $z = 4.79$ , respectively (see Table 1).

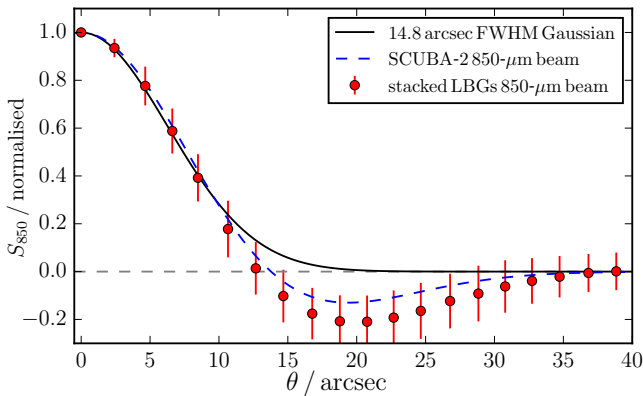


**Figure 3.** Light profile of the  $z \approx 3$  850- $\mu$ m stack from the left panel of Figure 2 (red points), compared with the SCUBA-2 850- $\mu$ m beam (dashed blue line) of Geach et al. (2017) and a 14.8 arcsec FWHM Gaussian (black solid curve). The stacked profile is consistent with the beam and therefore any contribution from clustering of associated sources must be on scales below 15'' if present at all.

### 3 RESULTS

#### 3.1 SED fitting

To fit the stacked flux densities we use 185 SED templates compiled by Swinbank et al. (2014). These include local galaxy templates from Chary & Elbaz (2001), Rieke et al. (2009) and Draine et al. (2007), as well as high-redshift starburst galaxies from Ivison et al. (2010) and Carilli et al. (2011), with a range of dust temperatures spanning 19-60 K. With redshifts fixed at the peak values from Table 1 we find the best-fitting SEDs using a standard  $\chi^2$  minimisation approach. At  $z = 4.79$  only the 850- $\mu$ m stacked flux density was detected at  $>3\sigma$  and so here we adopt our  $z = 3.87$  best-fitting SED redshifted to  $z = 4.79$  and normalised to

the 850  $\mu$ m flux. The fits have a consistent temperature of  $T_d \approx 40$  K.

We also determine the best-fitting rest-frame UV-to-mm model SEDs, where the UV-through-NIR photometry and uncertainties are medians and median absolute deviations for all LBGs in the redshift bin. We use the ‘energy balance’ code CIGALE<sup>2</sup> (Noll et al. 2009; Serra et al. 2011), adopting the Bruzual & Charlot (2003) stellar population templates with a double-burst, exponentially declining star formation history (SFH) in which the dependence of star formation rate on time is

$$\Psi(t) \propto \exp(-t_1/\tau_1) + f_m \exp(-t_2/\tau_2), \quad (7)$$

with  $\tau_1$ ,  $\tau_2$  and the mass fraction of the late burst population,  $f_m$ , being free parameters. This allows a large variation of in SFH, allowing for both single-burst and double-burst, instantaneous, exponentially declining and continuous histories. Dust attenuation is implemented using Calzetti et al. (2000) prescriptions and thermal dust emission uses the model of Casey (2012), where the mid-infrared power-law slope and dust emissivity index are fixed at 2.6 and 1.6, respectively, while the temperature is allowed to vary between 20 and 80 K<sup>3</sup>. The best-fit SEDs are plotted in Figure 4 as black curves. Since CIGALE uses energy balance, the corresponding unattenuated stellar emission can be estimated, which we show in Figure 4 as blue curves.

#### 3.2 UV & IR luminosities and stellar masses

The CIGALE fits described above are used to estimate the average stellar mass of each sample. As noted by Dunlop

<sup>2</sup> <http://cigale.lam.fr/>

<sup>3</sup> Note, that the dust temperature in the Casey (2012) models is an effective temperature, which is significantly higher than the temperature corresponding to the peak of the thermal infrared emission (see Figure 2 in Casey 2012).

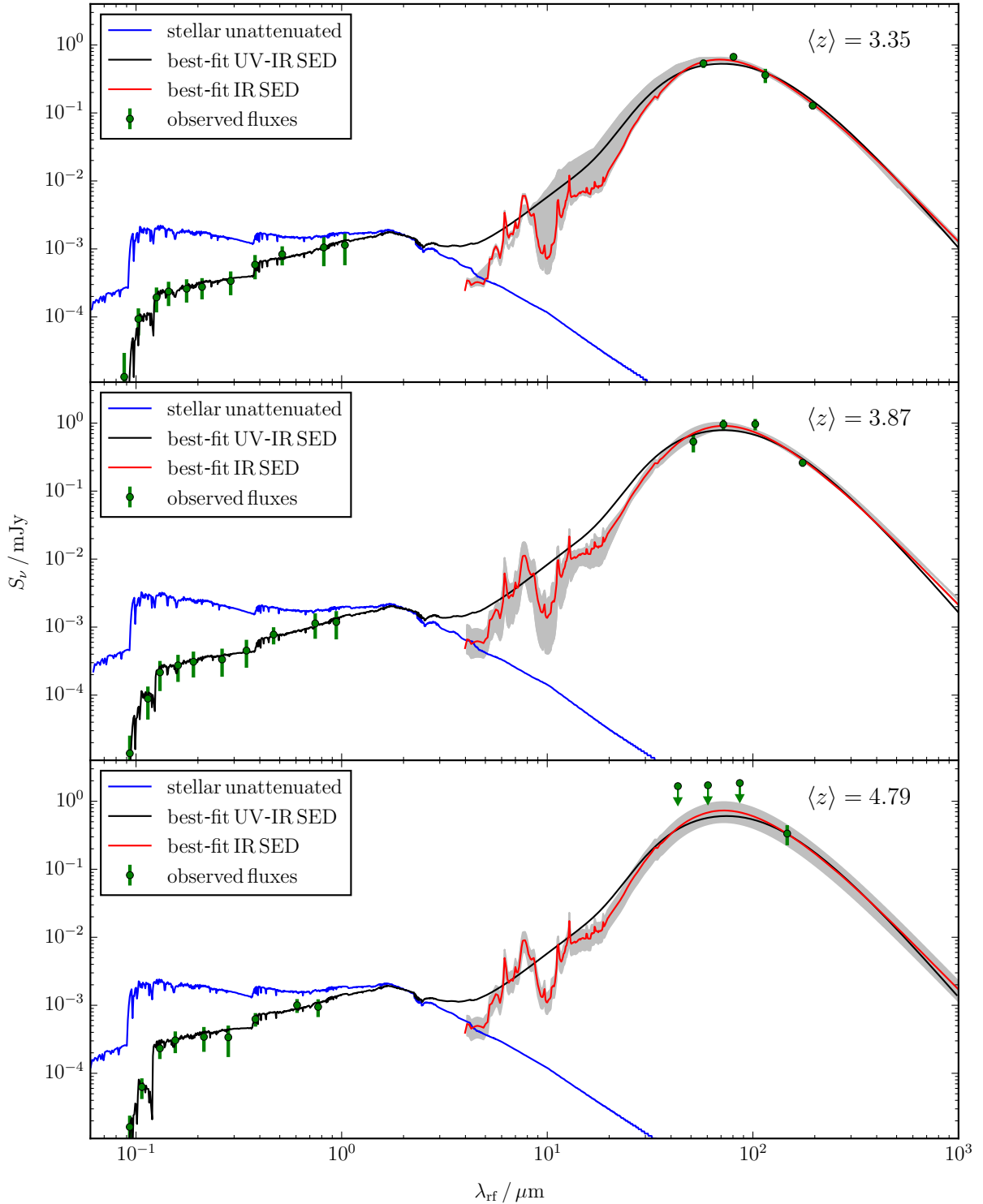


**Figure 4.** Best-fit SEDs at rest-frame wavelengths for the stacked results in each redshift bin. The IR photometry comes from stacking LBGs in *Herschel* SPIRE and JCMT SCUBA-2 850- $\mu\text{m}$  bands, while the rest-frame UV-NIR photometry points are median values from all the LBGs in a given redshift bin, with the errors being median absolute deviations. The red curves (used in the calculations of  $L_{\text{IR}}$ ) are best-fit empirical IR SEDs of Swinbank et al. (2014) found using a  $\chi^2$  minimisation method. In addition, we plot in black the best-fit rest-frame UV-mm SEDs found using CIGALE, where Bruzual & Charlot (2003) stellar population templates, Chabrier (2003) IMF, Calzetti et al. (2000) dust attenuation law and the thermal dust emission model of Casey (2012) were adopted (see Section 3.1 for details). Since CIGALE uses energy balance, we can find the amount of rest-frame UV dust reddening based on the IR luminosity and therefore estimate the unattenuated stellar emission SED, which we show here in blue.

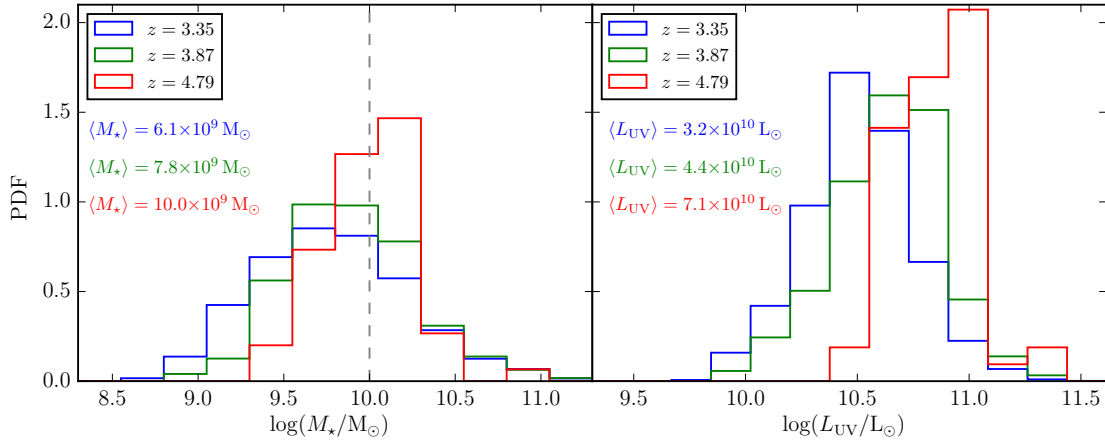


**Figure 5.** **Left:** Histogram of stellar masses for each redshift bin found from the best-fit rest-frame UV-NIR SEDs (see Section 3.2 for details). It can be seen that the masses increase with redshift, which is a consequence of the selection limit for our parent catalogue of  $K < 24.6$ . Since we can treat  $K$ -band as a rough proxy for the stellar mass (see Figure 6), we expect the average mass to increase with redshift due to the positive  $K$ -correction in this band. The grey dashed line marks the mass limit down to which our LBG sample is complete. This is a consequence of our parent optical catalogue being selected at  $K$ -band (see also Figure 6). **Right:** Histogram of the UV luminosities for each redshift bin in this work. As in the case of the stellar masses, the UV luminosities tend to increase with redshift. Again, this is caused by the depth of our parent catalogue in the rest-frame UV bands.

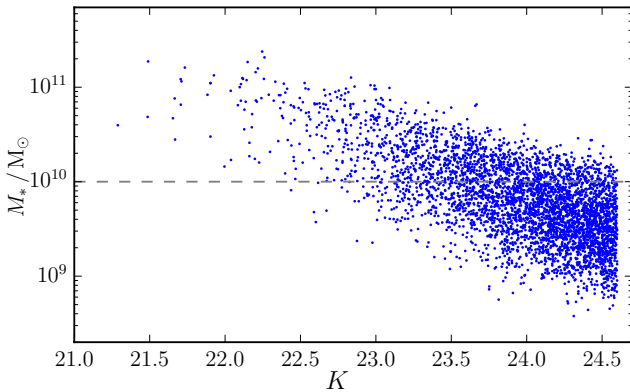


**Figure 6.** Stellar mass as a function of the  $K$ -band magnitude for the whole LBG sample used in this work. It can be seen that the  $K$ -band can be treated as a very rough proxy of the stellar mass. Applying a  $K$ -band cut of 24.6 (Section 2.1) at all 3 redshift bins causes slightly higher stellar masses to be selected at higher redshift bins, due to the positive  $K$ -correction (see Figure 5 and Table 2). The dashed grey line marks the mass completeness limit, being the consequence of our parent optical catalogue being selected at  $K$ -band.

(2011), the use of a multi-component SFH generally leads to more accurate values of stellar mass than the use of a single SFH. This is due to the fact that in a single burst scenario the entire stellar population must be young in order to reproduce the UV emission, thus the less massive but more abundant old stars are often not properly accounted for (see also Michałowski et al. 2012, 2014). The stellar mass distributions and corresponding mean values for each redshift bin are shown in Figure 5, with the numbers summarised in Table 2. The average stellar mass increases with redshift, which is a simple consequence of the NIR selection limit for

**Table 2.** Physical properties for LBGs. The stellar masses and UV luminosities are mean values in each bin (see Figure 5), with the errors being standard deviations rather than the errors on the mean (gives indication of the scatter). The IR luminosities are found by integrating the best-fit empirical IR templates (red curves in Figure 4) between 8 and  $1000\mu\text{m}$ .

$\langle z \rangle$	$\log(M_*/M_\odot)$	$\log(L_{\text{UV}}/L_\odot)$	$\log(L_{\text{IR}}/L_\odot)$
3.35	$9.78 \pm 0.45$	$10.51 \pm 0.25$	$11.36^{+0.14}_{-0.03}$
3.87	$9.89 \pm 0.38$	$10.65 \pm 0.27$	$11.64^{+0.05}_{-0.05}$
4.79	$10.00 \pm 0.27$	$10.85 \pm 0.17$	$11.69^{+0.12}_{-0.17}$

our parent catalogue (Section 2.1), as shown in Figure 6. For the same reason, our  $K$ -band limited sample is only complete to a stellar mass limit of  $\log(M_*/M_\odot) \gtrsim 10.0$  (see Figure 6).

The UV luminosity is defined here as  $L_{\text{UV}} \equiv \nu_{1600} L_{1600}$ , where the luminosity density at rest-frame  $1600\text{\AA}$ ,  $L_{1600}$ , is determined from the best-fitting SED. The luminosity distributions are shown in the right panel of Figure 5, with the mean values summarised in Table 2. Again,  $L_{\text{UV}}$  is increasing with redshift, which, as in the case of the stellar mass, is a result of the fixed optical flux limits in the LBG selection. While the difference between  $z = 3.35$  and  $z = 3.87$  is small ( $R < 27$  and  $i' < 27$  from Equations 1 and 2, respectively), the UV luminosity for  $z = 4.79$  is significantly higher because the corresponding rest-frame UV imaging is shallower ( $z' < 26$ , Equations 3 and 4).

Finally, total IR luminosities are determined by integrating under the best-fitting IR SED between rest-frame 8 and  $1000\mu\text{m}$  (Table 2). Again, average  $L_{\text{IR}}$  increases with redshift, which is most likely linked to the increase in stellar mass, rather than a real evolutionary trend.

**Table 3.** Stacking results for our LBG sample. In each  $\beta$  bin, the value of the UV slope is the unweighted average and the error bars correspond to the width of a given bin. A total number of LBGs in each  $\beta$  bin are given and the IRX values and errors are calculated using Equations 5 and 6, respectively. The stellar mass in each stellar mass bin is the mean with the error being the standard error on the mean. The lowest-mass bin upper limit is the only mass incomplete data point (see Figure 6).

Sample	N	$\langle \text{IRX} \rangle$
<b><math>\beta</math> bins :</b>		
$z = 3.35$		
$\beta = -2.00$	1523	$< 2.62$
$\beta = -1.63$	1420	$6.42 \pm 1.19$
$\beta = -1.09$	312	$17.75 \pm 4.21$
$\beta = -0.58$	111	$57.21 \pm 10.04$
$\beta = -0.03$	33	$77.46 \pm 21.56$
$z = 3.87$		
$\beta = -1.93$	228	$< 3.92$
$\beta = -1.57$	351	$7.76 \pm 1.62$
$\beta = -1.03$	81	$21.49 \pm 5.14$
$\beta = -0.48$	27	$< 44.92$
$z = 4.79$		
$\beta = -1.74$	50	$< 8.36$
$\beta = -1.11$	7	$19.78 \pm 6.10$
<b><math>M_*</math> bins :</b>		
$\log(M_*/M_\odot) = 9.47 \pm 0.13$	1339	$< 2.90$
$\log(M_*/M_\odot) = 9.90 \pm 0.13$	1633	$6.48 \pm 1.13$
$\log(M_*/M_\odot) = 10.33 \pm 0.13$	715	$23.08 \pm 2.39$
$\log(M_*/M_\odot) = 10.81 \pm 0.13$	157	$38.04 \pm 6.00$

## 4 ANALYSIS & DISCUSSION

### 4.1 IRX- $\beta$ relation

#### 4.1.1 UV slopes

Several different techniques have been used in the literature to measure the UV slope,  $\beta$  (see Rogers et al. 2013 for a review). The original work of Meurer et al. (1999) fitted a simple power-law to the ten continuum bands listed by Calzetti et al. (1994) in the rest-frame range of  $\sim 1250$ – $2500\text{\AA}$ . In most cases, however, only a few bands are available in that range, introducing uncertainty on  $\beta$ . In addition, the possible existence of the  $2175\text{\AA}$  feature in the dust attenuation curve can potentially impact the inferred values of the photometry-based UV slopes, driving up scatter in  $\beta$ . As shown by McLure et al. (2017) and explained further below, this scatter is significant enough to cause a bias that serves to flatten the IRX- $\beta$  relation. To try to minimise these effects, we measure  $\beta$  by fitting a power-law to the best-fitting SED over a rest-frame range of  $1250$ – $2500\text{\AA}$ , rather than the photometry directly.

#### 4.1.2 Stacking IRX

To measure the average  $\text{IRX} \equiv L_{\text{IR}}/L_{\text{UV}}$  we first bin the sample in  $\beta$ . We do not a priori know how  $L_{\text{IR}}$  couples with  $L_{\text{UV}}$ , so we cannot assume that the  $\langle \text{IRX} \rangle$  in each  $\beta$  bin is simply equal to  $\langle L_{\text{IR}} \rangle / \langle L_{\text{UV}} \rangle$ . Therefore we cannot stack the  $850\text{-}\mu\text{m}$  flux densities (i.e.  $L_{\text{IR}}$ ) and divide by the mean  $L_{\text{UV}}$ . Instead, we follow Bourne et al. (2017) by assuming that  $\langle \text{IRX} \rangle \equiv \langle L_{\text{IR}}/L_{\text{UV}} \rangle$ , stacking individual values of IRX,

**Table 4.** Functional forms of the IRX- $\beta$  relation for Calzetti-like attenuation and SMC-like extinction curves (see Section 4.1.3 for details) plotted in Figure 7.

$z$	IRX	$A_{1600}$
Calzetti-like attenuation curve		
3.35	$(1.56 \pm 0.06) \times (10^{0.4A_{1600}} - 1)$	$2.10(\beta + (2.31 \pm 0.07))$
3.87	$(1.53 \pm 0.05) \times (10^{0.4A_{1600}} - 1)$	$2.10(\beta + (2.34 \pm 0.07))$
4.79	$(1.57 \pm 0.11) \times (10^{0.4A_{1600}} - 1)$	$2.10(\beta + (2.31 \pm 0.10))$
SMC-like extinction curve		
3.35	$(1.53 \pm 0.04) \times (10^{0.4A_{1600}} - 1)$	$0.92(\beta + (2.37 \pm 0.03))$
3.87	$(1.51 \pm 0.03) \times (10^{0.4A_{1600}} - 1)$	$0.92(\beta + (2.37 \pm 0.03))$
4.79	$(1.59 \pm 0.13) \times (10^{0.4A_{1600}} - 1)$	$0.92(\beta + (2.39 \pm 0.16))$

which is more directly comparable to individually detected galaxies in the IR (eg. Capak et al. 2015; Koprowski et al. 2016). We find the individual values of  $L_{\text{IR}}$  by assuming all LBGs are described by the average best-fitting template, and normalise this to the observed  $850\mu\text{m}$  flux density at the position of each galaxy. Uncertainties on individual  $L_{\text{IR}}$  are estimated from the same measurement in noise-only maps at  $850\mu\text{m}$  using the same scaling factor. The results are presented in Figure 7 and Table 3.

We stress that here the individual values of IRX and  $\beta$  have been calculated independently and that we did not use the energy balance available in CIGALE. The  $L_{\text{IR}}$  for each LBG was found from the best-fit empirical dust-emission SEDs (red curves in Figure 4), while the  $L_{\text{UV}}$  and  $\beta$  were determined from the best-fit SED to the rest-frame UV-NIR photometry available for each of the sources in our sample. Although CIGALE uses the Calzetti et al. (2000) attenuation law, we emphasise that using the SMC-like extinction curve changes the resulting *intrinsic* stellar SEDs only, and has negligible effect on the inferred values of the UV slopes. To illustrate this, we also measure the observed UV slopes using an SMC-like extinction curve in our CIGALE fit (Figure 7).

#### 4.1.3 Functional form of IRX- $\beta$ relation

We adopt a functional form of IRX from Meurer et al. (1999)

$$\text{IRX} = (10^{0.4A_{1600}} - 1) \times B, \quad (8)$$

where  $A_{1600}$  is the attenuation at the rest-frame  $1600\text{\AA}$  in magnitudes and  $B$  is the ratio of two bolometric corrections

$$B = \frac{\text{BC}(1600)}{\text{BC}(\text{FIR})}. \quad (9)$$

The original Meurer et al. (1999) relation was defined as  $\text{IRX} \equiv L_{\text{FIR}}/L_{\text{UV}}$ , where

$$L_{\text{FIR}} = 1.25(L_{60} + L_{100}), \quad (10)$$

with  $L_{60}$  and  $L_{100}$  the luminosities measured by IRAS at 60 and  $100\mu\text{m}$ . To correct from  $L_{\text{FIR}}$  to total bolometric IR luminosity, the BC(FIR) correction was needed. Here we defined IRX as  $L_{\text{IR}}/L_{\text{UV}}$ , so the IR bolometric correction factor, BC(FIR), is by definition equal to unity. The

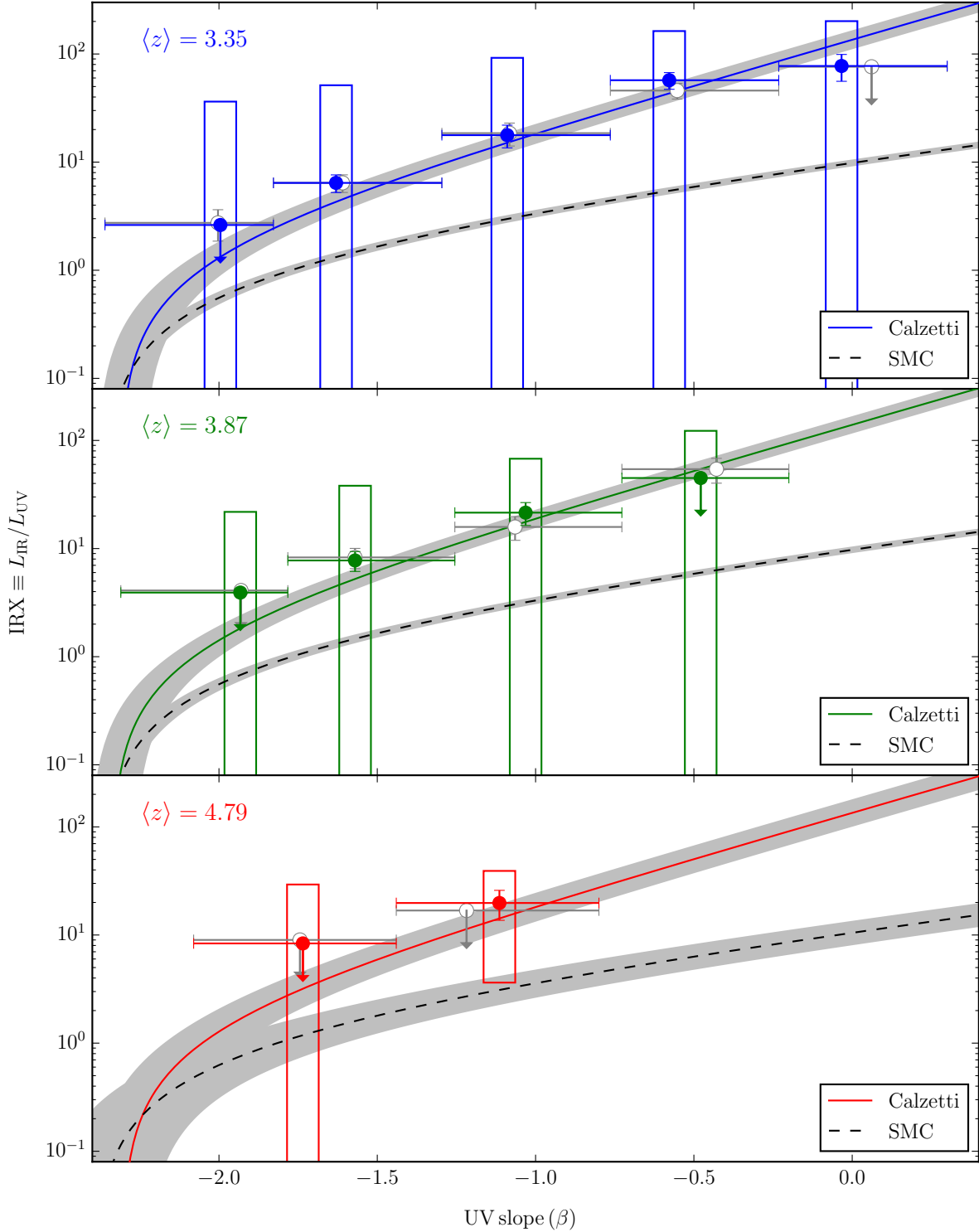


**Figure 7.** IRX- $\beta$  relation for each redshift bin studied in this work. UV slopes were determined from the best-fit SEDs to the rest-frame UV-NIR data only, where the Calzetti et al. (2000) attenuation curve was used (coloured points). Adopting the SMC-like curve affects the resulting intrinsic (before dust extinction) shape of the stellar emission SED only and has negligible effect on the inferred observed UV slopes. We show this by including data with UV slopes calculated using the SMC-like extinction curve (white points). The coloured points with error bars are the stacked values (Table 3), where we average the IRX values in each  $\beta$  and redshift bin (see Section 4.1.2 for details). The bars on  $\beta$  merely represent the widths of a given bin, while the values and errors on IRX were found using Equations 5 and 6, respectively (with  $3\sigma$  upper limits). The coloured rectangles depict the  $1\sigma$  scatter in the individual values of the IRX in each  $\beta$  bin. The curves depict the functional forms of the IRX- $\beta$  relation (Table 4), derived at each redshift bin for Calzetti- and SMC-like dust (see Section 4.1.3 for details). It is clear from this plot that our data are consistent with the Calzetti-like attenuation curve and that there is no obvious redshift evolution of the relation.

UV bolometric correction,  $BC(1600)$ , converts between all the stellar light available to heat the dust and the intrinsic  $F_{1600}$  measured at the rest-frame  $1600\text{\AA}$ . This can be calculated once the intrinsic stellar emission SED is known by integrating between the  $912\text{\AA}$  (Lyman limit) and infinity. As explained above however, to estimate the shape of the intrinsic stellar SED one needs to choose the form of the attenuation/extinction curve. The difference between the two is that the extinction law describes the effects of dust in the case of a screen between stars and observer and the attenuation law is characteristic of objects in which the dust is mixed with stars. Thus, attenuation laws also include the effects of scattering of the stellar light into our line-of-sight. We consider here two most extreme cases of Calzetti et al. (2000) attenuation curve and SMC-like extinction curve (Gordon et al. 2003).

To find the average intrinsic stellar emission SED corresponding to each of the attenuation/extinction curves, we used the energy balance feature of CIGALE, where the amount of the stellar light attenuated by dust is assumed to be equal to the light re-emitted in the IR (Table 2). The resulting UV bolometric corrections,  $BC(1600)$ , and the intrinsic UV slopes,  $\beta_{\text{int}}$ , for both attenuation/extinction curves for each redshift bin are given in Table 4.

The attenuation at  $1600\text{\AA}$ ,  $A_{1600}$  from Equation 8, can be described as

$$A_{1600} = \frac{\delta A_{1600}}{\delta \beta} (\beta_{\text{obs}} - \beta_{\text{int}}), \quad (11)$$

where  $\delta A_{1600}/\delta \beta$  is the slope of the reddening law and  $\beta_{\text{obs}}$  and  $\beta_{\text{int}}$  are the observed and the intrinsic UV slopes, respectively. To find the slope of the reddening law for the Calzetti- and SMC-like curves, we redden an intrinsic (dust unattenuated) stellar SED (blue curves in Figure 4) in small steps and calculate the amount of the attenuated stellar light. This is then equated with the energy re-emitted in the IR by dust. The results of this exercise are depicted in Figure 8, where we find slopes of 2.1 for the Calzetti- and 0.9 for the SMC-like dust.

The resulting functional forms of the IRX- $\beta$  relations (Equations 8, 9 and 11) for each attenuation/extinction curve in each redshift bin are summarised in Table 4 and plotted in Figure 7. As can be seen in Figure 7, assuming different attenuation/extinction laws does not affect the inferred values of IRX- $\beta$ , which is of course to be expected, since both UV slope and IRX are observables that should not depend on the model assumptions. It is therefore clear from Figure 7, that our data is consistent with the Calzetti-like dust attenuation, consistent with McLure et al. (2017), and that there is no significant evolution of the IRX- $\beta$  relation with redshift, as found for the submm-bright SCUBA-2 galaxies by Bourne et al. (2017). It is also clear from Figure 8, consistent with the models of Narayanan et al. (2017) and Popping et al. (2017), that galaxies following a given IRX- $\beta$  relation have similar stellar populations and similar intrinsic UV slopes.

## 4.2 Comparison with recent studies

In Figure 9 we compare our  $z = 3.35$  results with others works: Heinis et al. (2013); Álvarez-Márquez et al. (2016);

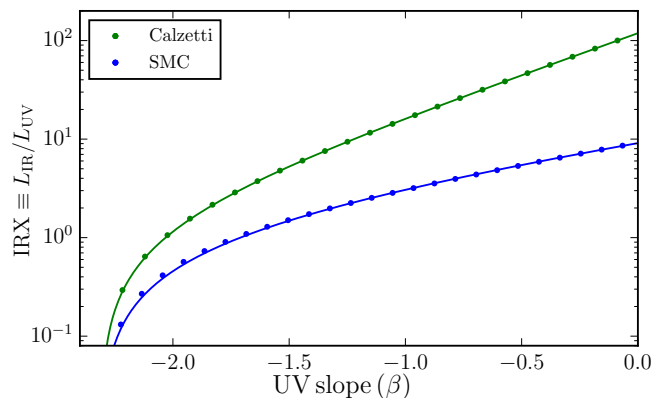


**Figure 8.** Infrared excess as a function of the observed UV slope for Calzetti-like attenuation and SMC-like extinction curves. The points represent the results of the simulations, wherein the unattenuated stellar emission SED was reddened using both, the Calzetti-like attenuation and SMC-like extinction curves in small steps. In each step the resulting IRX value was determined based on the balance between the energy attenuated in the rest-frame UV and re-emitted in the IR. The solid lines are the best-fit functional forms (Equation 8), with the resulting slopes of 2.1 and 0.92 for the Calzetti- and SMC-like dust, respectively (see Section 4.1.3 for details).

Reddy et al. (2017) and McLure et al. (2017). Solid and dashed black lines represent the functional forms of the IRX- $\beta$  relation for Calzetti-like attenuation and SMC-like extinction curves from Table 4. Systematic differences can be immediately noted. McLure et al. (2017) and the present work are consistent with Calzetti-like dust, while other work are intermediate between the Calzetti- and SMC-like curves. A potential reason for this inconsistency, pointed out by McLure et al. (2017) and noted earlier, is the relatively large uncertainty associated with the determination of the photometry-based values for UV slopes. Since the reddest  $\beta$  bins are populated by very few sources, a small number of overestimated UV slopes can cause an apparent drop in IRX, pushing values towards the SMC-like curve.

To investigate the effects of the scatter of the photometry-based UV slopes about their real values on the resulting shape of the IRX- $\beta$  relation, we have re-stacked our  $z = 3.35$  data. To estimate the UV slope for each galaxy, we fit a simple power-law to the photometry available in the rest-frame range of  $1250\text{-}2500\text{\AA}$  and then stack the IRX in the same  $\beta$  bins as in Section 4.1.2. The results are shown in Figure 9 as white circles. It can be seen that at the red end, IRX values are suppressed, effectively flattening to relation and pushing towards the SMC-like curve. This is because, with our present data, we only have three continuum bands in the rest-frame range of  $1250\text{-}2500\text{\AA}$ , resulting in larger errors on  $\beta$  and therefore more scatter in individual  $\beta$  bins. Using power-law fits to the corresponding rest-frame UV range in the best-fitting SEDs, using all 11 bands of observational data (even if this is not in the nominal range for a direct estimate of  $\beta$ ) reduces this scatter.

Another approach, taken by McLure et al. (2017), is to bin the sample in stellar mass. This is motivated by the growing consensus that it is the total stellar mass that influences the amount of the dust extinction (Heinis et al. 2013;

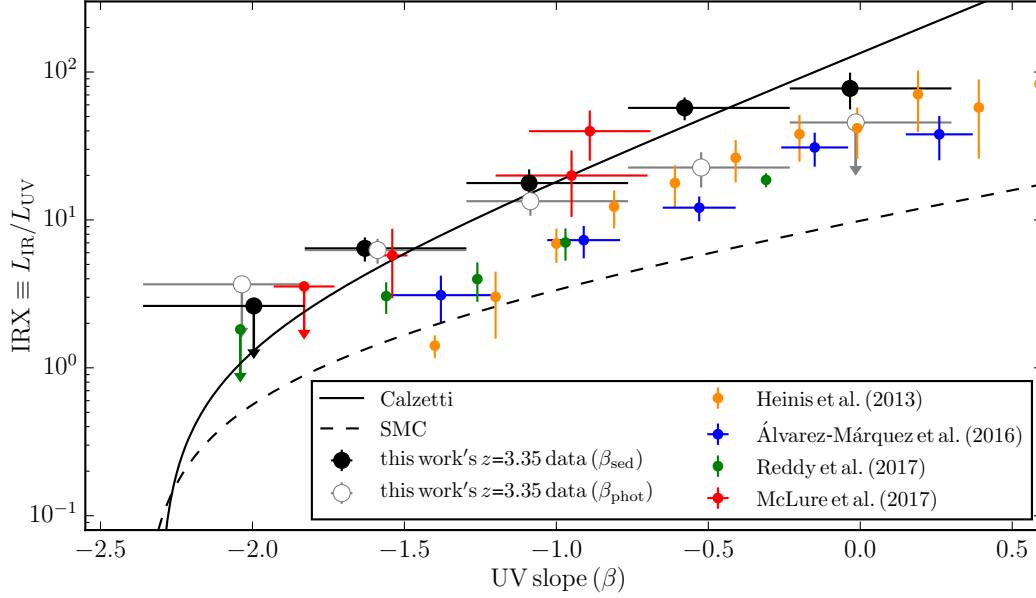


**Figure 9.** IRX- $\beta$  relation for  $z \sim 3$  LBGs for this work’s sample (black circles), compared with some of the recent literature results (Heinis et al. 2013; Álvarez-Márquez et al. 2016; Reddy et al. 2017; McLure et al. 2017). The black solid and dashed lines represent the Calzetti and SMC-like dust curves from Table 4. It is clear that, while ours and McLure et al. (2017) data is consistent with the Calzetti-like dust, others seem to be lying between two dust curves. As shown by McLure et al. (2017), this is caused by the uncertainties in the inferred values of the photometry-based UV slopes. We confirm this by including the data with  $\beta$ ’s determined from the best-fit power laws to the rest-frame 1250-2500Å photometry (white circles). One can clearly see that significantly larger errors on the photometry-based values of  $\beta$  flatten the slope of the corresponding IRX- $\beta$  relation (see Section 4.2 for details).

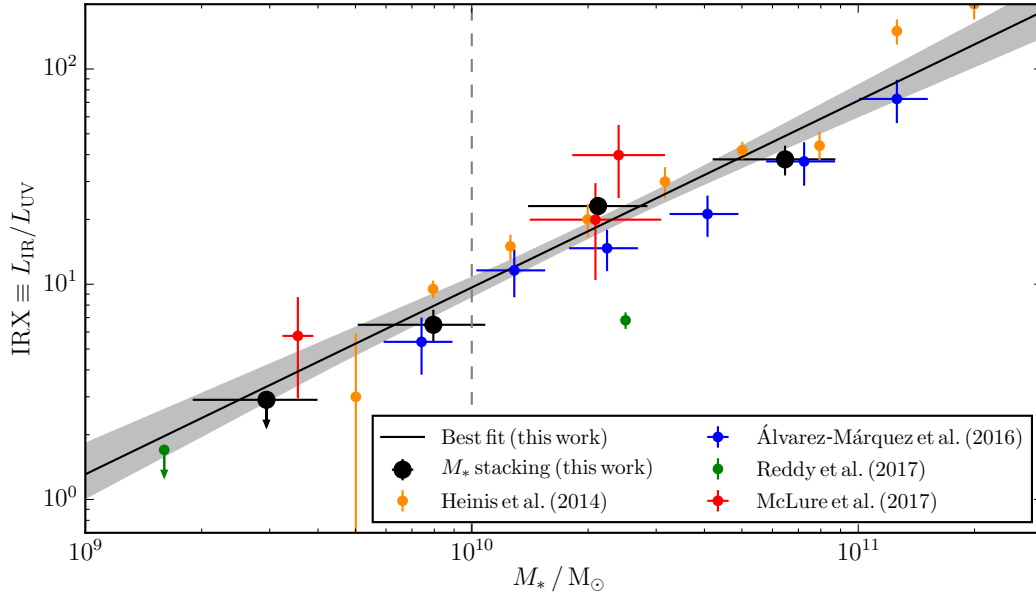


**Figure 10.** IRX- $M_*$  relation for our  $z \sim 3$  LBGs compared with recent literature results (Heinis et al. 2013; Álvarez-Márquez et al. 2016; Reddy et al. 2017; McLure et al. 2017) from Figure 9. It is clear that the rather striking systematic inconsistencies from Figure 9 now appear significantly decreased. This further confirms that the scatter in Figure 9 is mainly driven by different techniques of determining  $\beta$ . This is because in the IRX- $M_*$  relation, stellar masses are determined from the best-fit SEDs, with the corresponding errors of a very similar order (see Section 4.2 for details). The dashed line represents the mass limit down to which our LBG sample is complete. The lowest-mass upper limit is therefore the only mass-incomplete data point.

Álvarez-Márquez et al. 2016; Dunlop et al. 2017; Reddy et al. 2017). We show the stellar mass-binned results of McLure et al. (2017) in Figure 9 as red circles. It clearly shows, consistent with this work, that  $z \sim 3$  LBGs are affected by dust extinction characteristic of the Calzetti et al. (2000) law. With  $M_*$  being a more fundamental parameter, often the dependence of IRX on  $M_*$  is determined, instead of UV slope. To this end, we stack the  $z \approx 3$  sample in bins of  $M_*$ . The results are shown in Figure 10 as black circles, with a best-fitting power-law curve of

$$\log(\text{IRX}) = (0.87 \pm 0.10) \times \log(M_*/10^{10}M_\odot) + (0.98 \pm 0.04), \quad (12)$$

and the grey area depicting  $1\sigma$  uncertainties. Our results are in excellent agreement with McLure et al. (2017), who find a virtually identical form, with a slope of  $0.85 \pm 0.05$  and zero point of  $-0.99 \pm 0.03$ . We also compare to other results in the literature, corresponding to the data from Figure 9. One can see that the inconsistencies between different works are much smaller, most likely because the stellar masses are in all cases determined from the best-fit SEDs well-sampled with photometry.

## 5 CONCLUSIONS

We have extended the work of Coppin et al. (2015) to improve on and calibrate the IRX- $\beta$  relation at  $z \approx 3$ -5 using 4178 Lyman-break galaxies, stellar mass-complete down to a limit of  $\log(M_*/M_\odot) \gtrsim 10.0$ . We are able to determine the average total IR luminosity by stacking galaxies in deep SCUBA-2  $850\mu\text{m}$  and SPIRE  $250$ - $500\mu\text{m}$  imaging. By evaluating the observed UV slope,  $\beta$ , and emergent UV luminosity, we investigate the infrared excess, IRX, as a function of observed UV slope and stellar mass, deriving functional forms. We conclude:

(i)  $3 < z < 5$  LBGs are consistent with the Calzetti et al. (2000) attenuation law, consistent with the findings of McLure et al. (2017) at  $z \sim 3$ , now extended to  $z \sim 5$ . This describes a scenario where dust and stars are ‘well mixed,’ on average. In addition, similarly to Bourne et al. (2017), we find no significant redshift evolution in the IRX- $\beta$  over  $z \approx 3$ -5.

(ii) the IRX- $\beta$  relationship for LBGs in our sample is characteristic of galaxies with similar stellar population ages, corresponding to similar intrinsic UV slopes ( $\beta_{\text{intr}} \sim -2.3$ ), such that observed value of  $\beta$  are entirely driven by dust obscuration. In turn, this increases the corresponding IR luminosity and hence the IRX. This picture is consistent with the theoretical work of Narayanan et al. (2017) and Popping et al. (2017).

(iii) comparing our results with the recent literature findings of Heinis et al. (2013); Álvarez-Márquez et al. (2016); Reddy et al. (2017) and McLure et al. (2017) we find some inconsistencies, where some papers have found significantly lower IRX values for a given  $\beta$ , implying a more ‘SMC-like’ relation. We have confirmed, that these inconsistencies are driven by scatter in measured values of  $\beta$  from limited photometry which serves to artificially flatten IRX- $\beta$ . The scatter is significantly reduced by determining  $\beta$  from full SED fits, we resolve by determining the values of  $\beta$  from the

best-fit SEDs to the 11 rest-frame UV-NIR photometry data points.

(iv) by stacking IRX in bins of stellar mass, instead of as a function of  $\beta$  results in a much more consistent picture. There is a tight IRX- $M_*$  relation in which dust-reprocessed stellar emission scales nearly linearly with stellar mass. There is much better consistency across different works in this parameter space, likely due to the full SED fitting used to derive stellar masses, reducing relative uncertainties. We agree that the IRX- $M_*$  relationship is probably a far better proxy for correcting observed UV luminosities to total star formation rates, provided an accurate handle on  $M_*$  can be had, and also gives clues as to the physical driver of dust-obscured star formation in high-redshift galaxies.

## ACKNOWLEDGEMENTS

K.E.K.C. and M.P.K. acknowledge support from the UK’s Science and Technology Facilities Council (grant number ST/M001008/1). J.E.G. is supported by the Royal Society. M.J.M. acknowledges the support of the National Science Centre, Poland through the POLONEZ grant 2015/19/P/ST9/04010; this project has received funding from the European Union’s Horizon 2020 research and innovation programme under the Marie Skłodowska-Curie grant agreement No. 665778. KK acknowledge support from the Swedish Research Council and the Knut and Alice Wallenberg Foundation. NB acknowledges support from the European Research Council Advanced Investigator Program, COSMICISM (ERC-2012-ADG-20120216, PI R.J.Iverson).

## REFERENCES

- Álvarez-Márquez J., et al., 2016, *A&A*, **587**, A122  
 Baugh C. M., Lacey C. G., Frenk C. S., Granato G. L., Silva L., Bressan A., Benson A. J., Cole S., 2005, *MNRAS*, **356**, 1191  
 Bertin E., Arnouts S., 1996, *A&A Suppl.*, **117**, 393  
 Bian F., et al., 2013, *ApJ*, **774**, 28  
 Blaizot J., Guiderdoni B., Devriendt J. E. G., Bouchet F. R., Hatton S. J., Stoehr F., 2004, *MNRAS*, **352**, 571  
 Bourne N., et al., 2017, *MNRAS*, **467**, 1360  
 Bouwens R. J., et al., 2016, *ApJ*, **833**, 72  
 Brammer G. B., van Dokkum P. G., Coppi P., 2008, *ApJ*, **686**, 1503  
 Bruzual G., Charlot S., 2003, *MNRAS*, **344**, 1000  
 Calzetti D., Kinney A. L., Storchi-Bergmann T., 1994, *ApJ*, **429**, 582  
 Calzetti D., Armus L., Bohlin R. C., Kinney A. L., Koornneef J., Storchi-Bergmann T., 2000, *ApJ*, **533**, 682  
 Capak P. L., et al., 2015, *Nat*, **522**, 455  
 Caputi K. I., Cirasuolo M., Dunlop J. S., McLure R. J., Farrah D., Almaini O., 2011, *MNRAS*, **413**, 162  
 Carilli C. L., Hodge J., Walter F., Riechers D., Daddi E., Danerbauer H., Morrison G. E., 2011, *ApJ*, **739**, L33  
 Casey C. M., 2012, *MNRAS*, **425**, 3094  
 Casey C. M., et al., 2014, *ApJ*, **796**, 95  
 Chabrier G., 2003, *ApJ*, **586**, L133  
 Chapman S. C., Casey C. M., 2009, *MNRAS*, **398**, 1615  
 Chapman S. C., et al., 2000, *MNRAS*, **319**, 318  
 Chary R., Elbaz D., 2001, *ApJ*, **556**, 562  
 Chary R.-R., Pope A., 2010, preprint, ([arXiv:1003.1731](https://arxiv.org/abs/1003.1731))  
 Coppin K. E. K., et al., 2015, *MNRAS*, **446**, 1293  
 Dole H., et al., 2006, *A&A*, **451**, 417

- Draine B. T., et al., 2007, *ApJ*, **663**, 866
- Dunlop J. S., 2011, in Wang W., Lu J., Luo Z., Yang Z., Hua H., Chen Z., eds, *Astronomical Society of the Pacific Conference Series Vol. 446, Galaxy Evolution: Infrared to Millimeter Wavelength Perspective*. p. 209
- Dunlop J. S., et al., 2017, *MNRAS*, **466**, 861
- Fazio G. G., et al., 2004, *ApJS*, **154**, 10
- Fudamoto Y., et al., 2017, preprint, ([arXiv:1705.01559](https://arxiv.org/abs/1705.01559))
- Furusawa H., et al., 2008, *ApJS*, **176**, 1
- Geach J. E., et al., 2017, *MNRAS*, **465**, 1789
- Giavalisco M., 2002, *ARA&A*, **40**, 579
- Gordon K. D., Clayton G. C., Misselt K. A., Landolt A. U., Wolff M. J., 2003, *ApJ*, **594**, 279
- Griffin M. J., et al., 2010, *A&A*, **518**, L3
- Hartley W. G., et al., 2013, *MNRAS*, **431**, 3045
- Heinis S., et al., 2013, *MNRAS*, **429**, 1113
- Iverson R. J., et al., 2010, *MNRAS*, **402**, 245
- Kennicutt R. C., Evans N. J., 2012, *ARA&A*, **50**, 531
- Koprowski M. P., et al., 2016, *ApJ*, **828**, L21
- Kurczynski P., Gawiser E., 2010, *AJ*, **139**, 1592
- Lawrence A., et al., 2007, *MNRAS*, **379**, 1599
- Lo Faro B., Monaco P., Vanzella E., Fontanot F., Silva L., Cristiani S., 2009, *MNRAS*, **399**, 827
- Madau P., Dickinson M., 2014, *ARA&A*, **52**, 415
- Madau P., Ferguson H. C., Dickinson M. E., Giavalisco M., Steidel C. C., Fruchter A., 1996, *MNRAS*, **283**, 1388
- Magdis G. E., Rigopoulou D., Huang J.-S., Fazio G. G., Willner S. P., Ashby M. L. N., 2008, *MNRAS*, **386**, 11
- Magdis G. E., Rigopoulou D., Huang J.-S., Fazio G. G., 2010, *MNRAS*, **401**, 1521
- McLure R. J., et al., 2017, preprint, ([arXiv:1709.06102](https://arxiv.org/abs/1709.06102))
- Meurer G. R., Heckman T. M., Calzetti D., 1999, *ApJ*, **521**, 64
- Michałowski M. J., Dunlop J. S., Cirasuolo M., Hjorth J., Hayward C. C., Watson D., 2012, *A&A*, **541**, A85
- Michałowski M. J., Hayward C. C., Dunlop J. S., Bruce V. A., Cirasuolo M., Cullen F., Hernquist L., 2014, *A&A*, **571**, A75
- Mortlock A., et al., 2013, *MNRAS*, **433**, 1185
- Narayanan D., Dave R., Johnson B., Thompson R., Conroy C., Geach J. E., 2017, preprint, ([arXiv:1705.05858](https://arxiv.org/abs/1705.05858))
- Noll S., Burgarella D., Giovannoli E., Buat V., Marcillac D., Muñoz-Mateos J. C., 2009, *A&A*, **507**, 1793
- Oke J. B., Gunn J. E., 1983, *ApJ*, **266**, 713
- Oliver S. J., et al., 2012, *MNRAS*, **424**, 1614
- Oteo I., et al., 2013, *A&A*, **554**, L3
- Ouchi M., et al., 2004, *ApJ*, **611**, 660
- Overzier R. A., et al., 2011, *ApJ*, **726**, L7
- Pentericci L., Grazian A., Scarlata C., Fontana A., Castellano M., Giallongo E., Vanzella E., 2010, *A&A*, **514**, A64
- Pilbratt G. L., et al., 2010, *A&A*, **518**, L1
- Planck Collaboration et al., 2016, *A&A*, **594**, A13
- Popping G., Puglisi A., Norman C. A., 2017, preprint, ([arXiv:1706.06587](https://arxiv.org/abs/1706.06587))
- Reddy N. A., Steidel C. C., 2009, *ApJ*, **692**, 778
- Reddy N. A., Steidel C. C., Fadda D., Yan L., Pettini M., Shapley A. E., Erb D. K., Adelberger K. L., 2006, *ApJ*, **644**, 792
- Reddy N. A., et al., 2017, preprint, ([arXiv:1705.09302](https://arxiv.org/abs/1705.09302))
- Rieke G. H., et al., 2004, *ApJS*, **154**, 25
- Rieke G. H., Alonso-Herrero A., Weiner B. J., Pérez-González P. G., Blaylock M., Donley J. L., Marcillac D., 2009, *ApJ*, **692**, 556
- Rigopoulou D., et al., 2006, *ApJ*, **648**, 81
- Rigopoulou D., et al., 2010, *MNRAS*, **409**, L7
- Rogers A. B., McLure R. J., Dunlop J. S., 2013, *MNRAS*, **429**, 2456
- Sawicki M., Yee H. K. C., 1998, *AJ*, **115**, 1329
- Scoville N., et al., 2016, *ApJ*, **820**, 83
- Serjeant S., et al., 2010, *A&A*, **518**, L7
- Serra P., Amblard A., Temi P., Burgarella D., Giovannoli E., Buat V., Noll S., Im S., 2011, *ApJ*, **740**, 22
- Shapley A. E., Steidel C. C., Adelberger K. L., Dickinson M., Giavalisco M., Pettini M., 2001, *ApJ*, **562**, 95
- Shapley A. E., Steidel C. C., Erb D. K., Reddy N. A., Adelberger K. L., Pettini M., Barmby P., Huang J., 2005, *ApJ*, **626**, 698
- Simpson C., et al., 2006, *MNRAS*, **372**, 741
- Simpson C., et al., 2012, *MNRAS*, **421**, 3060
- Somerville R. S., Primack J. R., Faber S. M., 2001, *MNRAS*, **320**, 504
- Stark D. P., Ellis R. S., Bunker A., Bundy K., Targett T., Benson A., Lacy M., 2009, *ApJ*, **697**, 1493
- Steidel C. C., Giavalisco M., Pettini M., Dickinson M., Adelberger K. L., 1996, *ApJ*, **462**, L17
- Swinbank A. M., et al., 2014, *MNRAS*, **438**, 1267
- Ueda Y., et al., 2008, *ApJS*, **179**, 124
- Verma A., Lehnert M. D., Förster Schreiber N. M., Bremer M. N., Douglas L., 2007, *MNRAS*, **377**, 1024

This paper has been typeset from a  $\text{\TeX}/\text{\LaTeX}$  file prepared by the author.